PAPER

Check for updates

Synthesis of 5-hydroxymethylfurfural from glucose using a *tert*-butoxyapatite catalyst

Hemant S. Kulkarni,[a] Paresh A. Kamble,[a] Chathakudath P. Vinod, [ID] [b] Virendra K. Rathod [ID] [a] and Mannepalli Lakshmi Kantam [ID] *[a]

In this study, 5-hydroxymethylfurfural (5-HMF) was obtained from glucose using *tert*-butoxyapatite, a heterogeneous catalyst. The *tert*-butoxyapatite catalyst was prepared and characterized by several techniques, such as XRD, SEM, TEM, EDS, elemental mapping HR-TEM, N_2-adsorption/desorption, XPS, and FT-IR. Several parameters were studied, such as temperature, catalyst loading, and glucose concentration. The *tert*-butoxyapatite catalyst having both acidic and basic sites gave a maximum glucose conversion of 87% with a 48% yield of HMF at 160 °C using 20 wt% catalyst in 12 h. Reusability studies of the catalyst are also presented.

1. Introduction

The advancement of human civilization has heavily relied on the utilization of fossil fuel reservoirs.[1] Currently, fossil fuels such as coal, petroleum, and natural gas are crucial in synthesizing value-added chemicals and fuels. However, the increasing demand for fossil fuels, combined with a significant rise in petrochemical prices due to the rapid depletion of oil reserves and heightened environmental concerns, has prompted a shift towards renewable resources as a viable alternative.[2] Biomass offers a renewable feedstock that addresses challenges associated with fossil fuel depletion and global warming.[3] Comprising starch, sugar, oil crops, and animal manure, biomass emerges as an economically viable and renewable resource, making it an exceptional alternative to fossil fuel-derived products.[4] Biomass sourced from agricultural residues, wood, and herbaceous crops primarily consists of biopolymers, including cellulose (35–50%), hemicellulose (25–30%), and lignin (25–30%).[5] The polysaccharides, namely cellulose and hemicellulose, can undergo hydrolysis, producing sugars, namely glucose and fructose, offering avenues for their conversion into value-added chemicals.[6] Thus, the exploration of sustainable and economically viable product development from biomass represents a significant research domain.[3]

HMF, also known as 5-hydroxymethylfurfural, is a chemical that holds tremendous appeal in this regard. HMF has been identified as one of the top 10 value-added chemicals by the US Department of Energy.[7] There is a wide scope in the market for HMF derivatives, though HMF itself has a limited market because of its low stability. HMF retains all six carbon atoms that were present in the hexoses. HMF features an aldehyde group located at the C2 position, a hydroxymethyl group situated at the C5 position, and a reactive furan ring, which collectively enable a broad range of potential functionalization and chemical transformations. HMF undergoes several reactions, such as hydration, oxidation, amination, esterification, and hydrogenation, to synthesize a wide variety of derivatives and platform chemicals.[8] Although HMF possesses a restricted market due to its inherent low stability, significant potential exists for its derivatives in the market. These derivatives include furan-based compounds such as 2,5-furan dicarboxylic acid,[7,9] 2,5-dimethylfuran,[10] 2,5-diformylfuran, and 5-hydroxymethylfuroic acid, as well as non-furanic compounds like adipic acid, levulinic acid, 1,6-hexanediol, caprolactone, and caprolactam.

Thus, the efficient synthesis of HMF is crucial not only for advancing research but also for producing polymers, fuel components, pharmaceuticals, and various other sectors. Glucose and fructose serve as starting materials for the synthesis of HMF. Fructose typically yields higher amounts of HMF due to its rapid dehydration *via* Brønsted acid sites.[11,12] In contrast, the dehydration of glucose to HMF presents more challenges. Nevertheless, glucose is considered a more favorable candidate for HMF production owing to its lower cost and greater availability.[13,14] Synthesis of HMF from glucose involves a two-step reaction pathway, which includes the conversion of glucose to fructose and subsequent fructose dehydration to produce HMF. Scheme 1 depicts the possible reaction for glucose dehydration to 5-HMF.

[a]Department of Chemical Engineering, Institute of Chemical Technology, Mumbai, 400019, India. E-mail: lk.mannepalli@ictmumbai.edu.in
[b]Catalysis and Inorganic Chemistry Division, CSIR-National Chemical Laboratory, Dr Homi Bhabha Road, Pune-411008, India
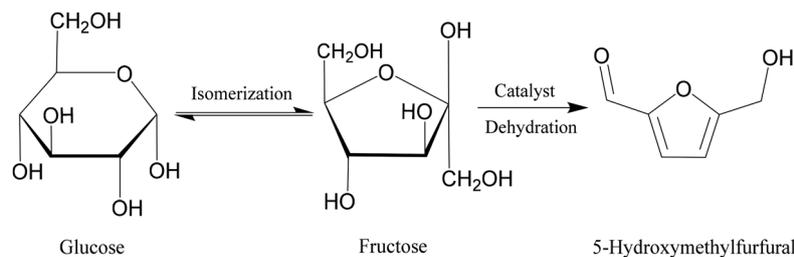
Scheme 1 Conversion of glucose to HMF.

It is crucial to design a catalytic system for isomerizing glucose to fructose, subsequently leading to the synthesis of HMF. Various reaction systems have been investigated for this objective, including organic solvents, biphasic systems, ionic liquids, and conventional acids. However, these systems present drawbacks such as increased energy consumption by organic solvents, high costs associated with ionic liquids, and potential corrosion or reactor damage when using conventional acids like HCl. Thus, employing heterogeneous catalysts for this purpose offers significant advantages due to their cost-effectiveness and easy recovery.[15]

In a study by Watanabe et al., an HMF yield of 20% and a glucose conversion of 81% were achieved in hot compressed water at 200 °C for 5 minutes using anatase TiO_2 as a catalyst. Additionally, the catalytic potential of ZrO_2 was examined under identical reaction conditions, resulting in a 5.2% HMF yield and a 47% conversion of glucose.[16] Ohara et al. investigated the efficacy of a hybrid catalytic system for synthesizing HMF in DMF. They achieved the highest HMF yield of 42% with a 73% conversion of glucose using a catalyst comprising hydrotalcite/Amberlyst 15 (2 : 1 w/w).[17] This result was obtained under the reaction conditions of 80 °C for 9 hours, with 3 wt% glucose. Yan et al. observed a yield of 47% for HMF when utilizing an $SO_4^{2-}/ZrO_2/Al_2O_3$ catalyst in DMSO at a temperature of 130 °C.[18] Liu et al. documented and achieved an HMF yield of 41% under the conditions of 140 °C for 2 hours using an Al_2O_3–B_2O_3 catalyst with an Al/B ratio of

5 : 5.[19] Jiménez-López et al. synthesized a novel mesoporous tantalum phosphate catalyst (MTP). Under the reaction conditions of 170 °C for 1 hour within a water–MIBK biphasic system, the catalyst achieved a maximum yield of 32.8% for HMF with 56.3% glucose conversion.[15] Table 1 presents a comparison between the current study and previous research on the dehydration of glucose to HMF.

Apatites are extensively employed in heterogeneous catalysis for a variety of chemical reactions, including oxidation,[20,21] reduction,[22] C–C bond formation,[23,24] cycloaddition,[25,26] N-arylation,[27] epoxidation,[28] water gas shift reaction,[29] and hydroformylation.[30] The primary characteristic of apatite surfaces is their acid–base properties, which play a crucial role in catalysing organic synthesis reactions. TBAP is a form of hydroxyapatite in which the OH group is replaced by a tertiary-butoxy (t-OBu) group. Like hydroxyapatite (HAP), TBAP contains both acidic and basic sites: Ca^{2+} ions act as Lewis acidic sites, while the oxygen atoms in PO_4^{3-} and OH^- groups serve as Lewis basic sites, and the P–O–H groups provide Brønsted acidity.[31–33] In this research, we demonstrate that tert-butoxyapatite, abbreviated as TBAP in DMSO solvent, acts as an effective catalyst for the gram-scale conversion of glucose to HMF. The TBAP catalyst is heterogeneous, allowing for easier separation from the reaction mixture compared to homogeneous catalysts. This innovative catalytic system paves the way for a novel process that will enable the industrial-scale synthesis of HMF directly from glucose.

Table 1 Dehydration of glucose to 5-HMF catalyzed by heterogeneous catalysts

Sr. no.	Glucose (g)	Catalyst	Solvent	Catalyst loading (wt%)	T (°C)	Time (h)	Glucose, %C	HMF, %S	HMF, %Y	Ref.
1	0.1	TiO_2	Water	100	250	0.083	39	71	27	34
2	0.1	TiO_2–ZrO_2	Water	100	250	0.083	44	67	29	35
3	0.1	ZrO_2	Water	100	200	0.083	48	11	5	36
4	0.09	Hydrotalcite/Amberlyst 15 (2 : 1 w/w)	DMSO	300	80	3	41	61	25	17
5	0.1	SO_4^{2-}/ZrO_2–Al_2O_3 (Zr/Al = 1 : 1 n/n)	DMSO	20	130	15	100	48	48	18
6	0.05	Al_2O_3–B_2O_3 (Al/B = 5 : 5)	DMSO	40	140	2	—	—	41.4	19
7	0.1	SO_4^{2-}/ZnO	DMSO	50	160	6	96	—	35	37
8	0.2	SnPCP@MnO_2-PDA	DMSO	25	150	5	—	60	55.8	38
9	0.15	Mesoporous tantalum phosphate	Water/MIBK	33	170	1	56.3	—	32.8	15
10	0.26	Sn-Mont	THF/DMSO	75	160	3	98	—	53.5	39
11	0.36	PS-PEG-OSO_3H	Water/DMSO (1 : 2)	55	120	1	98	—	84	40
12	0.223	MIL-SO_3H	Water : THF (39 : 1 V/V)	22	130	24	—	—	29	41
13	0.04	SAPO-34	GVL/water	50	170	0.66	—	—	93.6	42
14	1	TBAP-8	DMSO	20	160	12	87	70	48	This work

2. Materials and methods

2.1 Materials

Godavari Biorefineries Ltd supplied HMF. Glucose was obtained from S.D. Fine Chemicals, while potassium *tert*-butoxide and ammonium fluoride were procured from Thomas Baker Pvt. Ltd; calcium nitrate and sodium chloride (NaCl) were purchased from Oxford Lab Fine Chemicals, Ltd. Tetrahydrofuran (THF) was procured from Sisco Laboratory Chemicals Pvt. Ltd.

2.2 Catalyst preparation

The coprecipitation method was employed for the preparation of the catalyst. A solution was prepared by dissolving $(NH_4)_2HPO_4$ (7.92 g, 0.06 mol) and KO^tBu (2.4 g, 0.02 mol) in 250 mL of water, maintaining the pH above 12 by the addition of 15–20 mL of ammonium hydroxide. This solution was then added dropwise to an aqueous solution of $Ca(NO_3)_2 \cdot 4H_2O$ (23.6 g, 0.1 mol) in 150 mL of water under continuous stirring. The resulting suspension was stirred at 50 °C for 8 hours. The precipitate was separated by vacuum filtration, washed with doubly distilled water, and dried in an oven at 60 °C. The synthesized catalyst was designated as TBAP-8. TBAP-4 and TBAP-12 were similarly prepared except for the aging time, which varied to 4 and 12 hours, respectively.[43] Additionally, the hydroxyapatite (HAP) and fluoroapatite (FAP) were prepared according to Choudary and Kantam, with a modification in the ageing time to 8 hours.[43]

2.3 Catalyst characterization

XRD studies were conducted using a PANalytical Empyrean instrument in the 2θ range of 5°–80°. The morphological properties of the catalyst were investigated by scanning electron microscopy (SEM) using a Carl Zeiss Model Supra 55 with an accelerating voltage of 5.00 kV and transmission electron microscopy using an FEI Tecnai T20 with an accelerating voltage of 200 kV. The crystal structure of the catalyst was studied using high-resolution transmission electron microscopy and Selected Area Electron Diffraction (SAED) analysis using an FEI Tecnai T20. The elemental constitution and the elemental mapping of the catalysts, in terms of Ni loading, were determined by energy-dispersive X-ray spectroscopy (EDS) using a Carl Zeiss Model Supra 55. The functional groups of the catalysts were identified by Fourier transform infrared spectroscopy (FT-IR) using a Bruker FTIR 80 V instrument. The specific surface area and the porosity of the catalysts were analyzed by N_2 adsorption/desorption analysis using a Quanta-Chrome Novae 2200 instrument. Boehm acid–base titration was employed to assess the surface acidity and basicity of the catalyst. For the acidity determination, 0.5 g of the catalyst was submerged in 25 mL of a 0.05 N NaOH solution and stirred for 24 hours. The resulting suspension was then filtered and washed. Subsequently, 10 mL of the filtrate was titrated with 0.05 N HCl, using phenolphthalein as an indicator. The surface acidity was calculated based on the volumes of NaOH and HCl used in the titration. To measure the basicity, 0.5 g of the catalyst was immersed in 25 ml of a 0.05 N HCl solution and stirred for 24 hours. After filtration and washing, 10 ml of the filtrate was titrated with a 0.05 N NaOH solution. The chemical states of the catalyst were analyzed by X-ray photoelectron spectroscopy (XPS) using a Thermo K-Alpha Plus spectrometer with a monochromated Al-Kα source ($E = 1486.6$ eV). The charge neutralization gun was switched on throughout the data acquisition. Furthermore, the binding energy of the samples was cross-checked and referenced to adventitious C 1s at 284.6 eV.

2.4 Experimental method

A 25 mL round-bottom flask with a reflux condenser and magnetic stirrer was submerged in an oil bath with a PID controller. The flask was then submerged in an oil bath, which utilized a PID controller to regulate the temperature. For the experiment, 1 g of glucose and 10 mL of DMSO were introduced into the flask, heated to a desired temperature, and the catalyst was added. After the designated reaction time, the mixture was cooled to room temperature.

The products were analyzed using High Performance Liquid Chromatography (HPLC) with a Refractive Index (RI) detector. HMF was detected using an Agilent Hi-Plex column (4.6×250 mm), and the mobile phase was H_2SO_4 (0.005 mol L^{-1}) with a flow rate of 0.3 mL min^{-1}. Fig. S1–S5 shows chromatograms of the reaction mass (pre-isolation), isolated HMF, standard sample of glucose, HMF, and levulinic acid.

The conversion of glucose, the selectivity, and yield of HMF are calculated and defined according to the following formula:

$$\text{Glucose Conversion} (\%) = \frac{\text{moles of converted glucose}}{\text{moles of starting glucose}} \times 100\% \tag{1}$$

$$\text{HMF selectivity} (\%) = \frac{\text{moles of produced HMF}}{\text{moles of converted glucose}} \times 100\% \tag{2}$$

$$\text{HMF yield} (\%) = \frac{\text{moles of produced HMF}}{\text{moles of starting glucose}} \times 100\%. \tag{3}$$

2.5 HMF isolation method

A standard liquid–liquid extraction technique using tetrahydrofuran (THF) as the extraction solvent was utilized to isolate HMF from the reaction mixture. Initially, the catalyst was separated from the reaction mixture *via* centrifugation for 30 minutes. Subsequently, a 10% aqueous sodium chloride (NaCl) solution was introduced to the separated mixture, resulting in the precipitation of a black solid, presumably humin. The precipitated humin was then separated through centrifugation for 30 minutes, followed by washing with water and drying in an oven at 60 °C. After drying, the mass of the humin was measured. Post-humin removal, 5-HMF was extracted from the remaining supernatant through liquid–liquid extraction (LLE). This extraction was conducted in a separating funnel, where THF was added to the supernatant, the mixture was shaken for approximately one minute, and phase

separation was allowed for one hour. This process yielded two distinct liquid layers: an upper THF layer and a lower aqueous layer. The addition of NaCl to the aqueous phase enhanced the partition coefficient between the organic and aqueous layers, thereby facilitating phase separation.[44] This extraction procedure was repeated for three cycles. Thereafter, THF was removed using a rotary evaporator, and the purity of 5-HMF was determined through HPLC analysis.[37] Despite undergoing distillation, the isolated sample still exhibited the presence of DMSO.

3. Results and discussion

3.1. Catalyst characterization

Fig. 1A presents the X-ray diffraction (XRD) patterns of TBAP-4, TBAP-8, TBAP-12, and HAP. The diffraction peaks observed by all TBAP catalysts are in good agreement with the standard data from the JCPDS file no. 00-055-0592, confirming the successful synthesis of the desired phase. The catalysts exhibit a hexagonal crystalline structure, as evidenced by the distinct peaks at $2\theta = 31.7°$, $32.13°$, $33°$, and $34.21°$, and the corresponding planes are (211), (112), (300), and (202), respectively.[22,45,46] Notably, the diffraction peaks associated with the (211), (112), and (300) planes become more pronounced as the Ca/P ratio increases, indicating enhanced crystallinity. This trend is further supported by calculated crystallinity values (Table 2) with TBAP-12 displaying sharper peaks than TBAP-4. Additional diffraction peaks are observed at $26°$, $29°$, $39.8°$, $46.8°$, $48.17°$, $49.6°$, and $53.3°$ corresponding to the

(002), (210), (310), (222), (312), (213), and (004) planes, respectively, providing further evidence of the hexagonal phase. The SEM images (Fig. 1B–E) of TBAP-8 reveal a plate-like morphology, characterized by irregularly shaped agglomerated, bulk-like particles and partially blocked pores. The Ca/P ratio for the TBAP-4, TBAP-8, and TBAP-12 catalysts was determined by energy-dispersive X-ray spectroscopy (EDS). As summarized in Table 2, the ratio increases with longer stirring duration, suggesting that the extended stirring enhances calcium incorporation within the catalyst structure.

The XRD patterns (Fig. 2A) of both fresh TBAP-8 and used TBAP-8 display similar diffraction profiles, suggesting the overall crystal structure remains largely unchanged after use. However, a slight reduction in the sharpness of the (211), (112), and (300) diffraction peaks in the used TBAP-8 may indicate a decrease in % crystallinity, likely due to a reduction in the Ca/P ratio as a result of calcium leaching after 5 cycles. SEM images (Fig. 2B and C) of both fresh and used catalysts reveal irregular-shaped particles with comparable surface morphology, indicating minimal structural degradation. Furthermore, the elemental mapping (Fig. S6 and S7) confirms the consistent presence of elements Ca, P, O, and C in both fresh and used catalysts, with no significant alteration in their spatial distribution, thereby supporting the material's structural stability upon repeated use.

Transmission electron microscopy (TEM) images of both fresh TBAP-8 (Fig. 3A and B) and used TBAP-8 (Fig. 3C and D) reveal agglomerated rod-like particles. The overall morphology remains consistent before and after use, with no significant structural changes observed. However, an increase in the par-
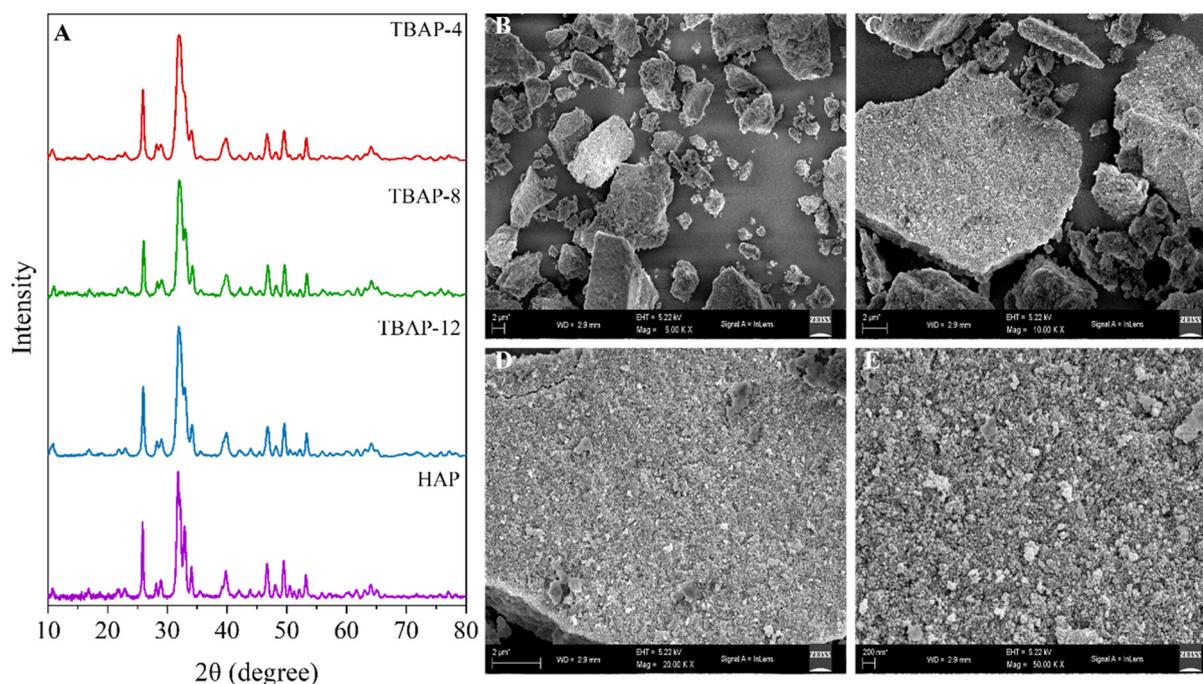

Fig. 1 The X-ray diffraction (XRD) spectra of (A) TBAP-4, TBAP-8, TBAP-12, and HAP (B−E) FE-SEM images of TBAP-8.

Table 2 EDS and Boehm titration data for TBAP catalysts

Catalyst	Ca/P (EDX)	S_{BET}, m^2 g^{-1}	V_p, cm^3 g^{-1}	d_p, nm	Total basicity, mole g^{-1}	Total acidity, mole g^{-1}	% crystallinity
HAP	1.7	40.2	0.4	17.03	—	—	84.3
TBAP-4	1.65	147.8	0.55	12.44	2.2	0.2	80.2
TBAP-8	1.87	131.6	0.5	12.24	2.3	0.17	80.6
TBAP-12	1.93	128.3	0.5	9.6	2.5	0.1	81.8
TBAP-8 (used)	1.62	86.3	0.24	12.21	—	—	80.0
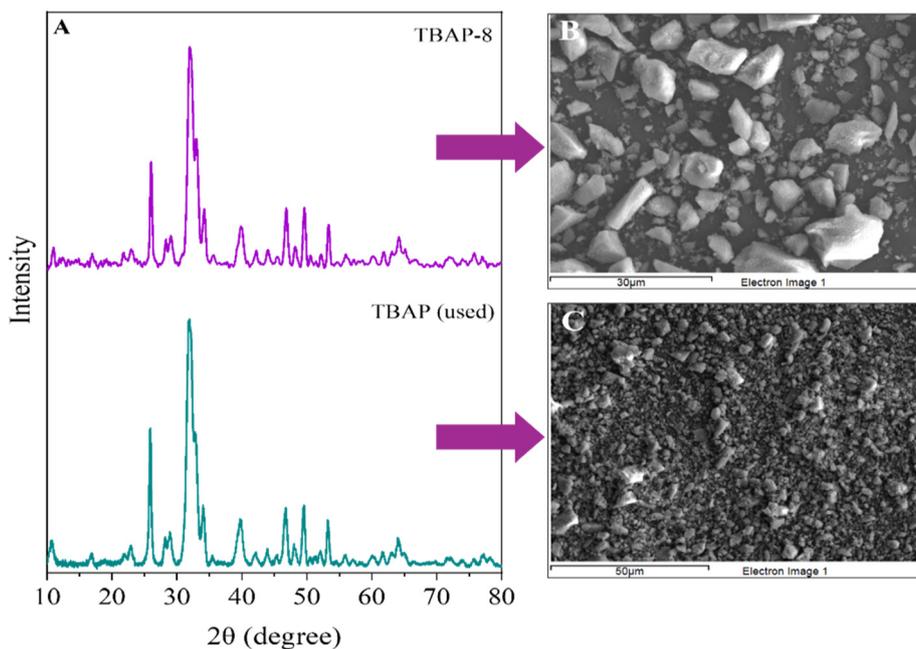
Fig. 2 (A) XRD diffractions of TBAP-8 and used TBAP-8 (after 5 cycles), (B) SEM image of TBAP-8, (C) SEM image of used TBAP-8 (after 5 cycles).

ticle size is noted- from 14.76 nm in fresh TBAP-8 to 16.63 nm in TBAP-8 catalysts used after 5 cycles, which may be attributed to the deposition of humin in the apatite structure. High-resolution transmission electron microscopy (HR-TEM) images and selected area electron diffraction (SAED) patterns (Fig. 4) for fresh and used samples display distinct lattice fringes characteristic of the apatite structure. These findings confirm the successful synthesis of the TBAP catalysts and demonstrate their structural integrity and stability.

Fig. 5 and Table S1 show FTIR analysis of TBAP catalysts in the 4000 cm^{-1} to 400 cm^{-1} range. TBAP-4 shows the presence of CO_3^{2-} vibrational stretching at 1420 cm^{-1}, indicating absorption of CO_2 from air.[22,47–49] The presence of CO_3^{2-} also confirms that the TBAP-4 is calcium-deficient apatite. The absence of CO_3^{2-} vibrational stretching in TBAP-8 and TBAP-12 indicates they are calcium-rich apatites. Thus, CO_3^{2-} vibrational frequencies dissipate with an increase in the stirring time from 4 h to 12 h. The presence of vibrational frequencies at 1425 cm^{-1} and 1452 cm^{-1} indicates the presence of B-type carbonated TBAP in TBAP-4 formed by replacing PO_4^{3-} with CO_3^{2-}.[48,49] A typical hydroxyapatite sample shows characteristic OH stretching vibration at 3574 cm^{-1} and OH bending vibration at 630 cm^{-1}.[50,51] In TBAP, the OH bending

vibration (630 cm^{-1}) disappears, and the OH stretching vibration shifts to 3537 cm^{-1} due to the incorporation of the *t*-OBu group.[50,52] Additionally, a band at 745 cm^{-1} suggests that the OH group participates in hydrogen bond formation [(CH$_3$)$_3$–O···H–O] due to the incorporation of the *t*-OBu group.[50–54] The PO_4^{3-} stretching frequency in all TBAP catalysts exhibits a strong absorption band at 1093 cm^{-1} and 1025 cm^{-1} corresponding to symmetrical stretching of P–O in PO_4^{3-}, along with absorption bands at 603 cm^{-1}, 571 cm^{-1}, and 471 cm^{-1} corresponding to the bending vibrational modes of P–O–P in PO_4^{3-}.[51,53] The stretching vibrational mode at 3628 cm^{-1} is ascribed to surface hydrogenophosphate (P–O–H) group, while the stretching vibrational mode at 3660 cm^{-1} suggests a bulk P–O–H group, indicating the presence of Brønsted acid (Fig. S8).[32]

Table 2 summarizes the elemental composition of TBAP catalysts based on their Ca/P ratio. The total acidity and basicity of these samples were determined through Boehm acid–base titration. The results indicate that a higher calcium content correlates with increased basicity, whereas a greater proportion of phosphorus content enhances the acidity of the catalyst. The elevated calcium content, likely a result of extended stirring times, leads to a high Ca/P ratio of 1.93 in
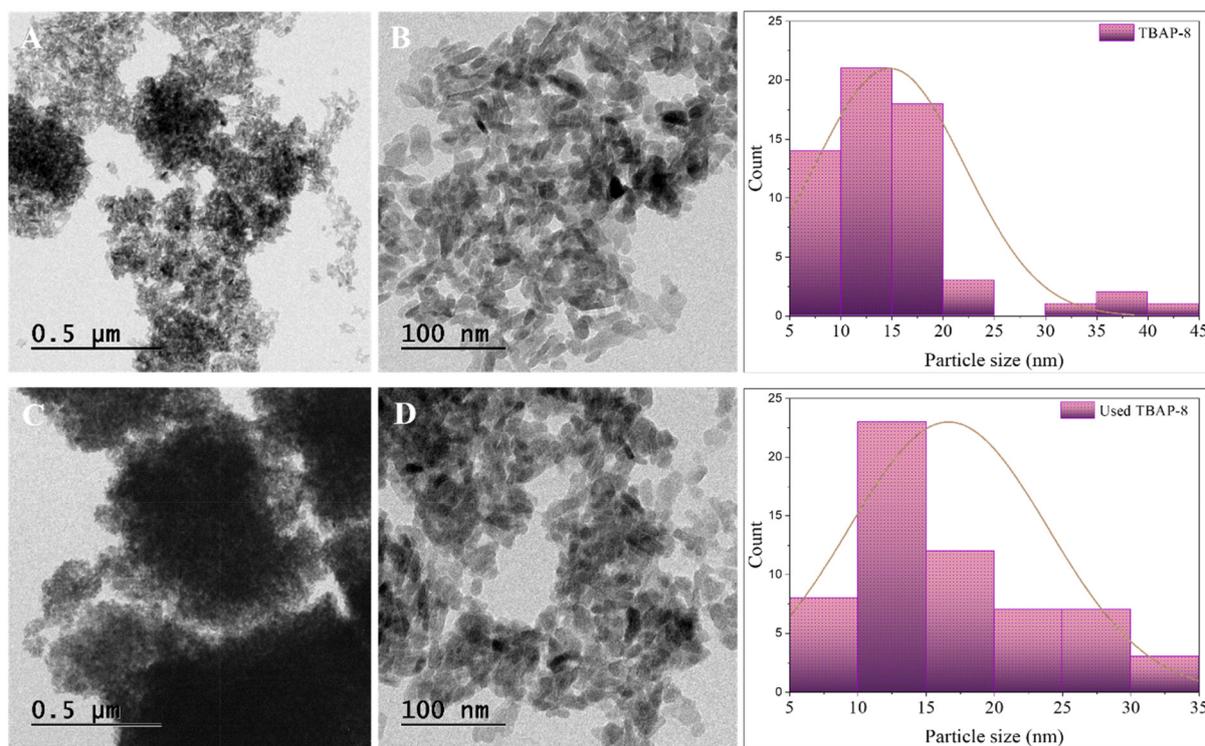
Fig. 3 TEM images and the particle size distribution of (A and B) TBAP-8 and (C and D) used TBAP-8 (after 5 cycles).
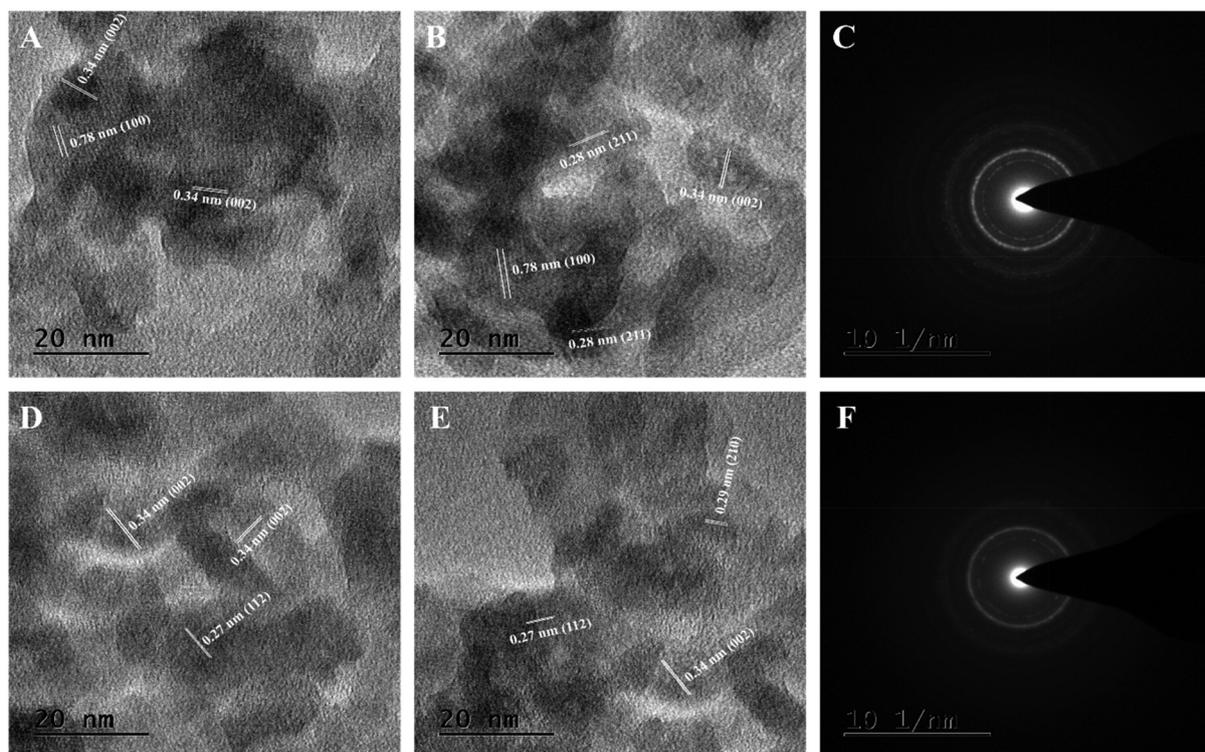

Fig. 4 HR-TEM images and SAED pattern of (A–C) TBAP-8 and (D–F) used TBAP-8 (after 5 cycles).
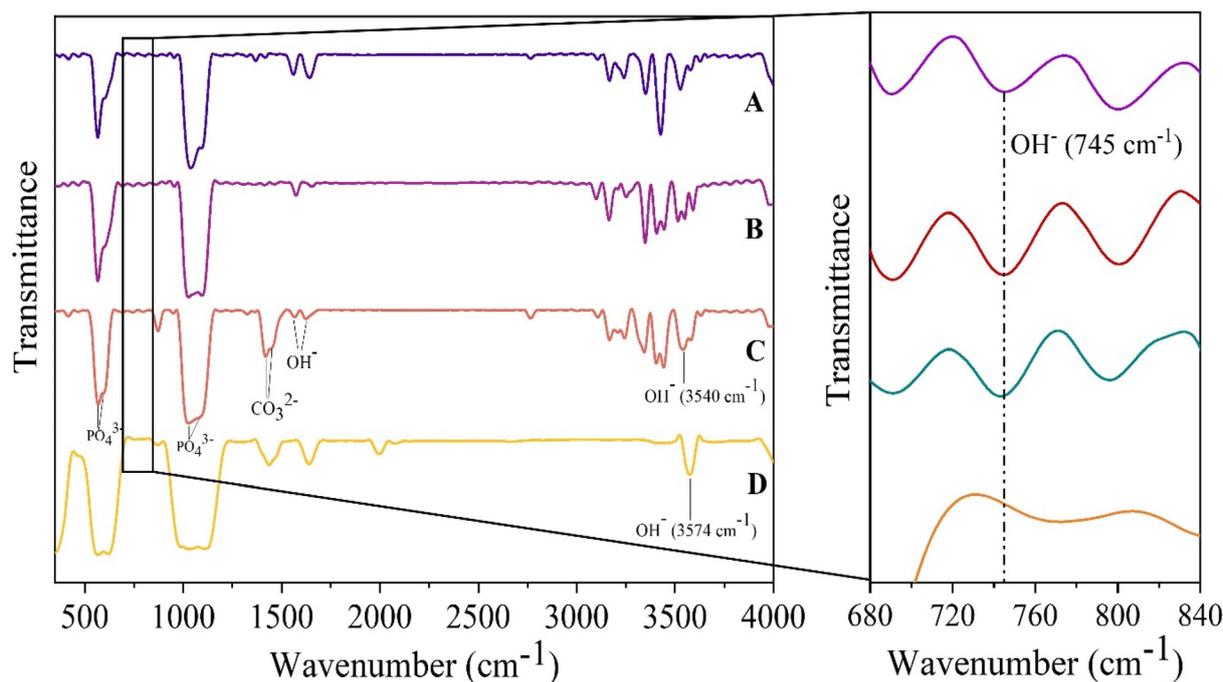
Fig. 5 FTIR analysis of TBAP catalysts (A) TBAP-12, (B) TBAP-8, (C) TBAP-4, and (D) HAP.

TBAP-12, reflecting a lower acidity. In contrast, TBAP-4, synthesized with a shorter stirring duration, exhibits a lower Ca/P ratio of 1.65 due to calcium deficiency. The lower calcium content corresponds to a relative enrichment in phosphorus content, making TBAP-4 more acidic than TBAP-8 and TBAP-12. These findings suggest that acidity can be effectively tuned by adjusting the Ca/P ratio, offering a strategy to control catalytic behavior through composition and synthesis parameters.

The specific surface area of the HAP, TBAP-4, TBAP-8, TBAP-12, and the used TBAP-8 catalysts were determined using Brunauer–Emmett–Teller (BET) analysis, as summarized in Table 2. Incorporation of the *t*-OBu group in the hydroxyapatite framework leads to an increase in the surface area. However, as the stirring time increased, a gradual decrease in the surface area was observed, which can be attributed to the higher concentration of calcium ions. This increase in calcium content elevates the Ca/P ratio from TBAP-4 to TBAP-12, resulting in a more compact structure and reduced surface area. For the used TBAP-8 catalyst, a decline in the surface area is noted, likely due to the accumulation of humin on the catalyst surface after repeated reaction cycles. Pore volume and pore diameter were assessed using the Barrett–Joyner–Halenda (BJH) method (Table 2). The introduction of the *t*-OBu group in the hydroxyapatite framework enhances the pore volume, which in turn contributes to a higher surface area in the TBAP catalysts. However, following 5 catalytic cycles, TBAP-8 exhibits a reduced pore volume, attributed to pore blockage caused by the accumulation of humins. While the pore volume increases with catalyst modification, the pore diameter tends to decrease, suggesting structural densification. The pore sizes of

all the catalysts fall within the range of 2 nm to 50 nm, characteristic of uniform mesoporous material.[22] The textural properties, including the N_2 adsorption–desorption isotherm and pore size distribution, are illustrated in Fig. 6. All the catalysts exhibit mesoporous characteristics with pore sizes between 2 nm to 20 nm.[22] According to IUPAC nomenclature, the isotherm corresponds to a type IV profile with an H1-type hysteresis loop, indicating the presence of uniform mesoporous structures composed of cylindrical or tubular pores.[55] The sharp initial uptake of N_2 at a relative pressure ($P/P0$) below 0.8 signifies the existence of micropores, while the pronounced hysteresis loop in the desorption branch confirms the presence of mesopores.[55] Notably, the reduced N_2 uptake at $P/P0 < 0.4$ in the used catalyst suggests a significant loss in pore volume, correlating with the observed decline in the surface area due to the accumulation of humin.

Fig. 7 presents the full X-ray Photoelectron Spectroscopy (XPS) survey spectra of TBAP-8. The survey confirms the presence of elements Ca (Ca 2p), P (P 2p), O (O 1s), and C (C 1s), indicating successful incorporation of key components into the catalyst structure. Fig. 8 further illustrates the high-resolution spectra of Ca (Ca 2p), P (P 2p), O (O 1s), and C (C 1s), detailing the chemical states and surface composition of catalysts TBAP-4, TBAP-8, and TBAP-12. The Ca 2p spectra (Fig. 8) exhibit characteristic spin–orbit splitting into Ca 2p3/2 and Ca 2p1/2 peaks, with binding energies from 347.2 eV and 350.5–350.8 eV, respectively. The energy separation between these peaks falls within the range of 3.3 eV–3.6 eV, consistent with the presence of Ca^{+2} in TBAP. These states suggest the coordination of a calcium atom to a phosphate group.[22,56] A secondary set of peaks is also observed at the binding energies
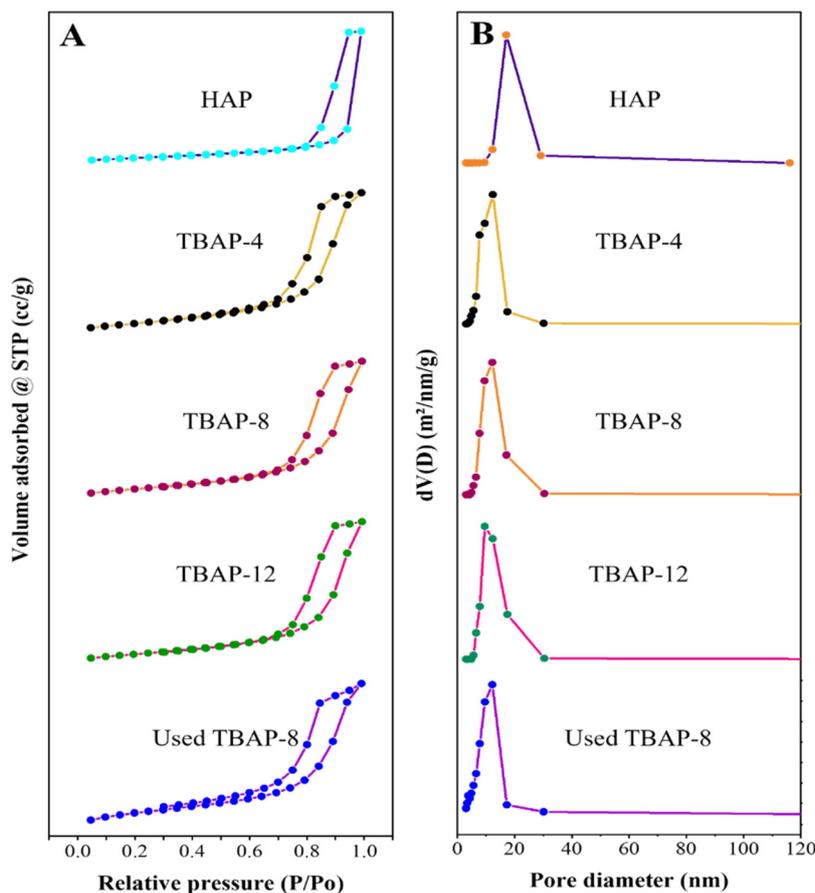
Fig. 6 N2 adsorption−desorption isotherms (A) and pore diameter distribution profiles (B) of TBAP catalysts.
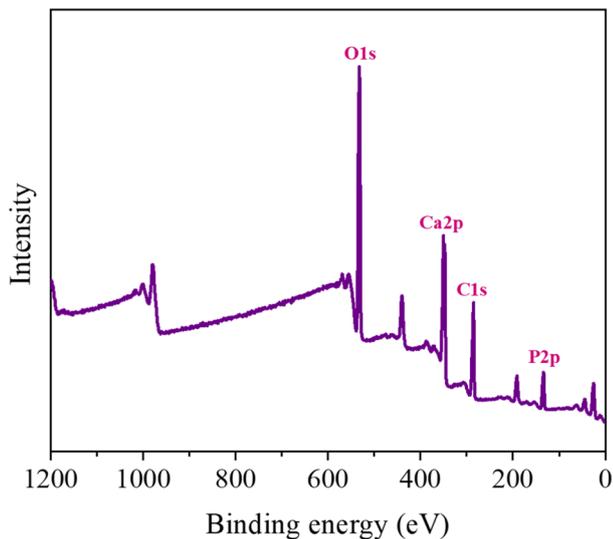

Fig. 7 XPS full survey spectra of TBAP-8.

of 348.8–349.4 eV (Ca 2p3/2) and 352.1–353.1 eV (Ca 2p1/2), respectively. The first doublet is attributed to apatite,[32,57] and the second doublet corresponds to calcium carbonate ($CaCO_3$), likely formed due to calcium deficiency on the catalyst surface.[57] Notably, the intensity of this second doublet diminishes as the Ca/P ratio increases, indicating a reduction in calcium vacancies. In all the catalysts, the P 2p region (Fig. 8) shows splitting into P $2p_{3/2}$ and P $2p_{1/2}$ at binding energies of 132.9–133.1 eV and 133.8–134.0 eV, respectively, with a spin–orbit splitting of 0.9 eV. These peaks are associated with the P^{+5} state of the phosphate group (PO_4^{3-}), tetrahedrally coordinated to an O atom.[57] Additionally, TBAP-4 and TBAP-8 exhibit a secondary contribution at binding energies of 135.4–135.6 eV (P $2p_{3/2}$) and 136.3–136.5 eV (P $2p_{1/2}$), respectively, and a spin energy difference of 0.9 eV. This second doublet is attributed to PO_3^-, and both PO_4^{3-} and PO_3^- environments are consistent with an apatite-like structure.[57] The dual doublets in TBAP-4 and TBAP-8 are likely due to the presence of surface carbonate species, which diminish in calcium-rich TBAP-12. The O 1s spectra reveal bonds designated as α, β, and γ (Fig. 8) corresponding to Ca–O, P–O, and C–O bonds. All catalysts exhibit peaks at 531.1–531.4 eV (α) and 533.1–533.7 eV (β) corresponding to the Ca–O and P–O bonds, respectively.[56,58] The more intense β peak in calcium-deficient TBAP-4 is attributed to the substitution of PO_4^{3-} by CO_3^{2-} groups. As the Ca/P ratio increases from TBAP-4 to TBAP-12, the β peak intensity decreases and shifts to lower binding energies, indicating a reduction of surface CO_3^{2-}
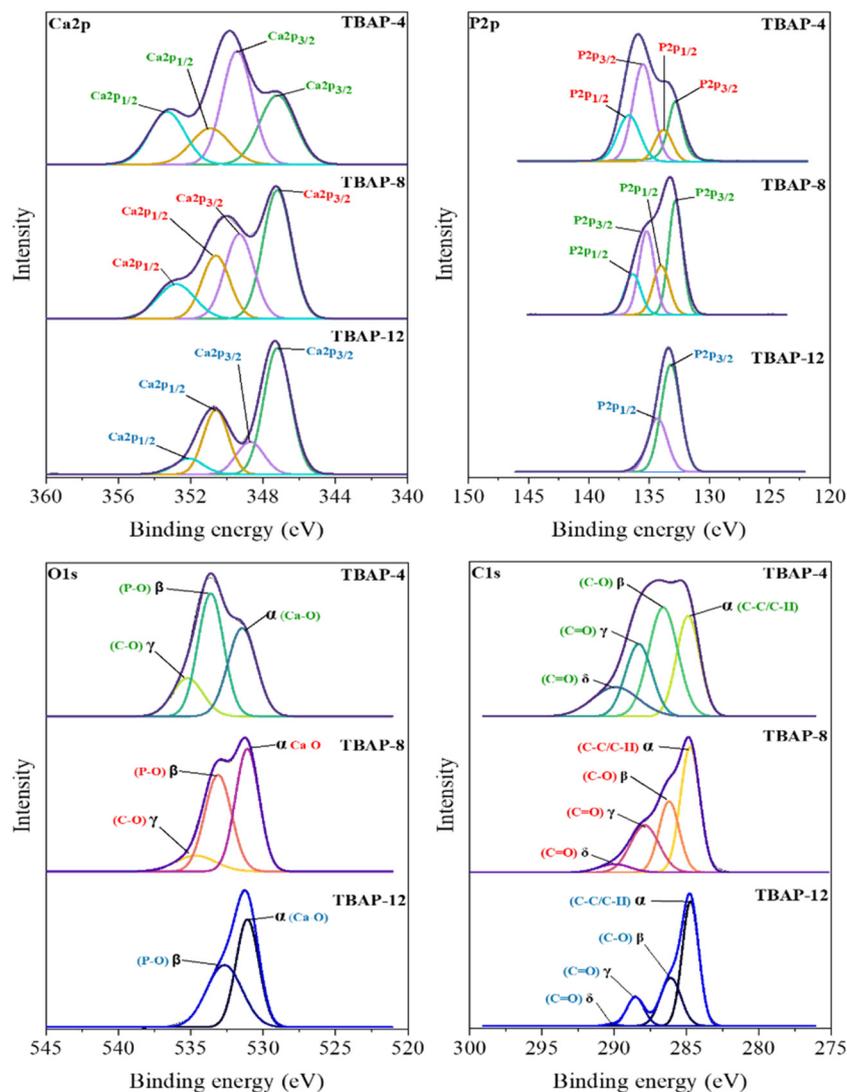
Fig. 8 Ca 2p, P 2p, O 1s, and C 1s spectra of TBAP catalysts.

groups. The γ peak, found at the binding energies at 535.2–535.7 eV and associated with CO_3^{2-} groups, also shifts and eventually disappears in TBAP-12, further suggesting decreasing surface carbonates with an increasing calcium content. Deconvolution of the C 1s spectrum (Fig. 8) reveals asymmetric peaks assigned as α (284.8 eV), β (286.1–286.6 eV), γ (288.0–288.5 eV), and δ (289.9–290.2 eV). The α and β peaks correspond to sp^3 C–C/C–H and C–O bonds. The β peak, indicative of C–O bonds from the *t*-OBu group in the *tert*-butoxy apatite catalysts and surface CO_3^{2-} species, formed by CO_2 adsorption from the ambient air, indicates calcium-deficient TBAP.[48,56,58] Similarly, the γ peak, representing C=O bonds, arises from the surface CO_3^{2-} species, linked to atmospheric CO_2. As the Ca/P ratio increases from TBAP-4 to TBAP-12, the intensity of the β and γ peak diminish, demonstrating that greater calcium content reduces CO_3^{2-} accumulation on the catalyst surface. This trend is reinforced by the δ peak, which fades with an increasing Ca/P ratio. Despite these

variations, the surface Ca/P ratio for all the catalysts remains approximately 1.3, lower than the ideal stoichiometric Ca/P ratio of 1.67. This discrepancy suggests persistent calcium deficiency at the catalyst surface, which correlates with the sustained presence of the γ peak across all the samples.

3.2. Catalytic activity

The conversion of glucose to HMF using TBAP occurs in two main steps (Fig. 9): (1) XPS analysis confirms the presence of Ca–O groups in TBAP, indicating the formation of Lewis acidic Ca^{2+} sites. During the isomerization of glucose to fructose, these Ca^{2+} sites catalyze the ring-opening of glucose pyranose to form a 1,2-enediol intermediate. This intermediate is stabilized by coordination with O–Ca–O and interactions with the DMSO solvent. The process facilitates further rearrangement and ring closure, ultimately yielding fructose, which can adopt a five-membered furanose ring structure. (2) FTIR analysis confirmed the presence of P–O–H groups, which serve as Brønsted
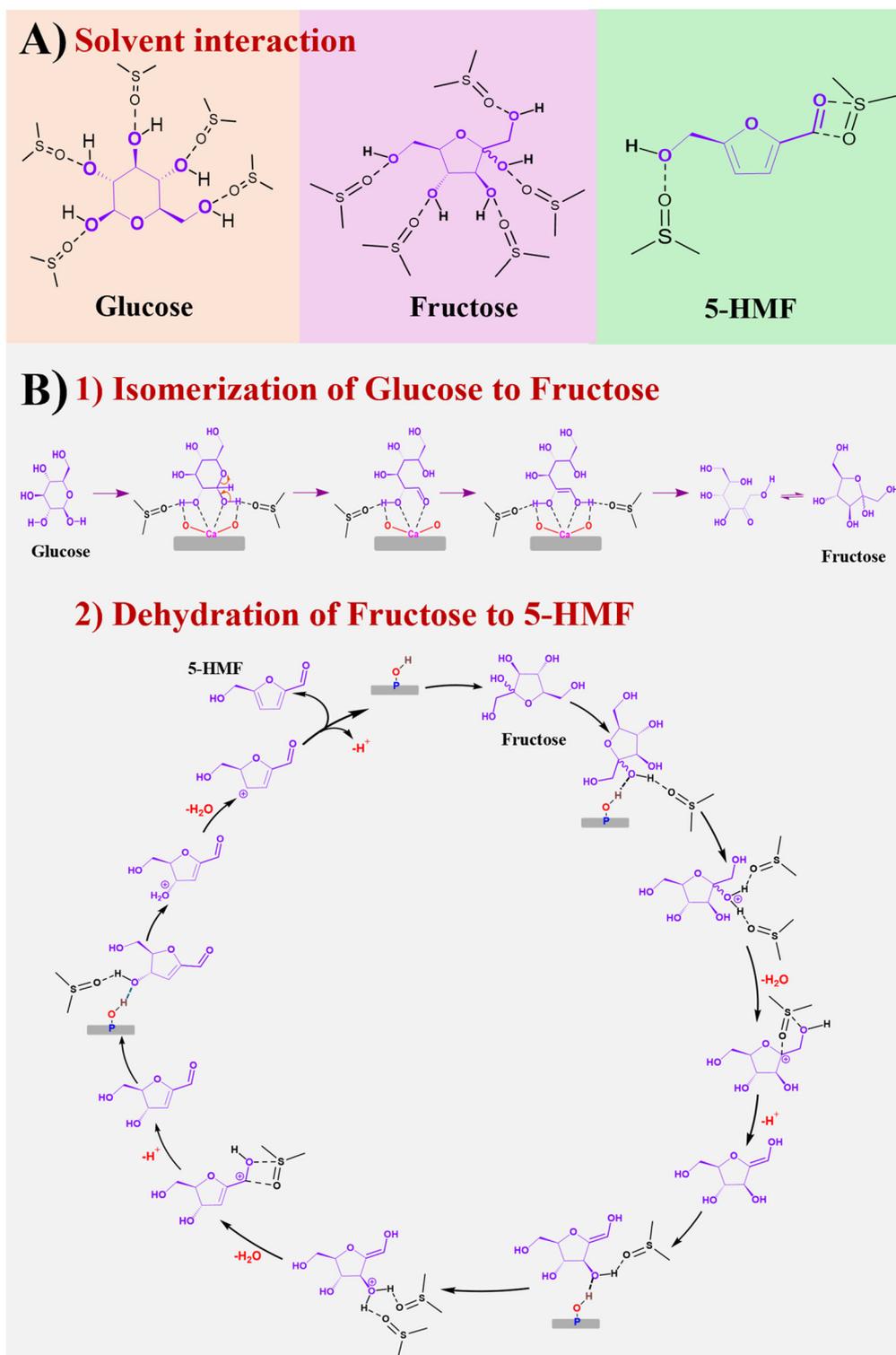
Fig. 9   (A) Solvent interaction with glucose, fructose, and 5-HMF, and (B) Plausible mechanism for the glucose to HMF reaction. Adapted from ref. 59–63.

acid sites by donating protons (H^+) during the dehydration of fructose to hydroxymethylfurfural (HMF). As reported in previous studies, these Brønsted acidic P–O–H sites facilitate the conversion of fructose to HMF.[42] Throughout the reaction, all

the intermediates were stabilized by DMSO, which also suppresses side reactions and improves the HMF yield.[59,60]

Various reaction parameters were investigated to achieve optimal conditions for glucose dehydration to HMF, aiming to

maximize both conversion and selectivity. Catalysts, designated as TBAP-4, TBAP-8, and TBAP-12, were synthesized using the co-precipitation method and subjected to aging periods of 4, 8, and 12 hours, respectively (Table 3). Of these, TBAP-8 exhibited superior performance, achieving a 48% yield of HMF and an 87% conversion of glucose. The superior performance of TBAP-8 is likely attributable to an optimal distribution of acidic and basic active sites, which promotes the isomerization of glucose to fructose, a critical intermediate step that also facilitates the subsequent dehydration to HMF. In contrast, the lower yield observed with TBAP-4 is attributed to the excessive formation of humins, resulting from higher acidity as compared to TBAP-8 and TBAP-12 (Table S2). The reduced activity of TBAP-12 is due to its lower concentration of acidic sites relative to TBAP-4 and TBAP-8, leading to an 84% conversion of glucose and a subsequent lower yield of 44%. Other apatites such as hydroxyapatite (HAP) and fluorapatite (FAP) were also utilized. Both the catalysts (HAP and FAP) afforded a lower yield of 5-HMF due to higher levulinic acid formation and lower conversion, respectively. The impact of catalyst loading on the conversion and selectivity of glucose and HMF was investigated using a previously optimized TBAP-8 catalyst (Table 4). Catalyst loading varied between 5–30 wt% relative to a fixed amount (1 g) of glucose. The data presented in the following table indicates that glucose conversion increases with the catalyst weight. Additionally, an increase in the catalyst amount correlates with a rise in humin formation (Table S3). Initially, HMF selectivity increases; however, beyond a catalyst quantity of 200 mg, a decline is observed. This decline is attributed to higher humin formation, which is caused by the increased number of acidic sites as the catalyst amount increases. The highest 5-HMF yield (48%) was achieved with a 20 wt% catalyst loading. Further increases in the catalyst loading (up to 30 wt%) resulted in a decrease in the HMF yield. Additionally, the formation of humins increased with greater catalyst quantities.

To achieve maximum glucose conversion and high selectivity for HMF, reactions were carried out within a temperature range of 100 °C to 170 °C using a TBAP-8 catalyst (Table 5). Glucose conversion and humin content increased with rising temperature. The yield of HMF was very low at low tempera-

Table 3 Effects of different catalysts
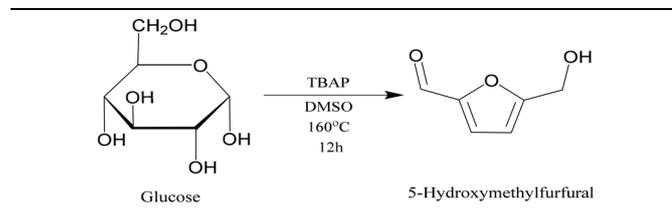
| Sr. no. | Catalyst | Glucose conversion (%) | Selectivity (%) | | HMF yield (%) |
			HMF	Levulinic acid	
1	HAP-8	72	23	53	—
2	FAP-8	55%	26	24	—
3	TBAP-4	80	64	7	38
4	TBAP-8	87	70	4	48
5	TBAP-12	84	62	4	44

Reaction conditions: glucose = 1 g, DMSO = 10 mL, catalyst quantity = 200 mg, temperature = 160 °C, time = 12 h.

Table 4 Effect of catalyst loading

| Sr. no. | Catalyst | Catalyst quantity (mg) | Glucose conversion (%) | Selectivity (%) | | HMF yield (%) |
				HMF	Levulinic acid	
1	TBAP-8	50	48	37	9	24
2		100	66	49	6	32
3		200	87	70	4	48
4		300	95	66	5	35

Reaction conditions: glucose = 1 g, DMSO = 10 mL, temperature = 160 °C, time = 12 h.

Table 5 Effect of reaction temperature

| Sr. no. | Catalyst | Temperature (°C) | Glucose conversion (%) | Selectivity (%) | | HMF yield (%) |
				HMF	Levulinic acid	
1	TBAP-8	100	17	8	19	2
2		120	29	12	12	7
3		140	41	28	9	18
4		150	73	59	7	42
5		160	87	70	4	48
6		170	93	66	4	15

Reaction conditions: glucose = 1 g, DMSO = 10 mL, catalyst quantity = 200 mg, time = 12 h.

Table 6 Effect of glucose concentration

| Sr. no. | Catalyst | Glucose (mg) | Glucose (mmol) | Glucose conversion (%) | Selectivity (%) | | HMF yield (%) |
					HMF	Levulinic acid	
1	TBAP-8	180	1	62	25	23	14
2		342	1.9	72	36	15	25
3		504	2.8	82	44	7	34
4		666	3.7	85	58	4	40
5		828	4.6	85	64	4	45
6		1000	5.5	87	70	4	48

Reaction conditions: DMSO = 10 mL, catalyst quantity = 20 wt%, temperature = 160 °C, time = 12 h.

tures, which instead favors the formation of levulinic acid and other side products. The yield of levulinic acid decreased as the temperature increased. At 100 °C, the glucose conversion was 17%, which increased to 93% at 170 °C. Table 5 shows that the yield of 5-HMF increased, peaking at 48% at 160 °C, before declining to 15% at 170 °C. The high temperature of 170 °C, combined with the presence of acidic sites, promotes rapid humin formation, which reduces the yield beyond 160 °C (Table S4).

A range of experiments was carried out to investigate how glucose concentration impacts conversion and selectivity. The experiments involved altering the glucose concentration, as shown in Table 6 and Table S5. As the glucose concentration increased from 1–5.5 mmol, it was observed that both conversion and selectivity for HMF increased. However, the selectivity for levulinic acid decreased. When the glucose concentration exceeds 3.7, there is a slight increase in the yield of HMF. The maximum yield of HMF, reaching 48%, was achieved when the glucose concentration was 5.5 mmol, with a reaction time of 12 hours at 160 °C.

3.3. Catalyst reusability study

A reusability test was conducted to evaluate the stability and activity of the catalyst (Fig. 10). After every cycle, the catalyst is removed from the reaction mixture by centrifugation, followed by a washing process with alcohol to eliminate impurities or the absorbed material. The catalyst is then dried overnight in an oven at 60 °C. Following this, a study on the reusability of the catalyst was conducted up to five cycles using optimized reaction parameters. As depicted in Fig. 10, the results indicate a minor decline in the yield with each successive cycle. This may be attributed to the accumulation of humin on the catalyst surface, which reduces the catalyst's activity. Nevertheless, the TBAP-8 catalyst demonstrates good stability for dehydrating glucose to HMF.
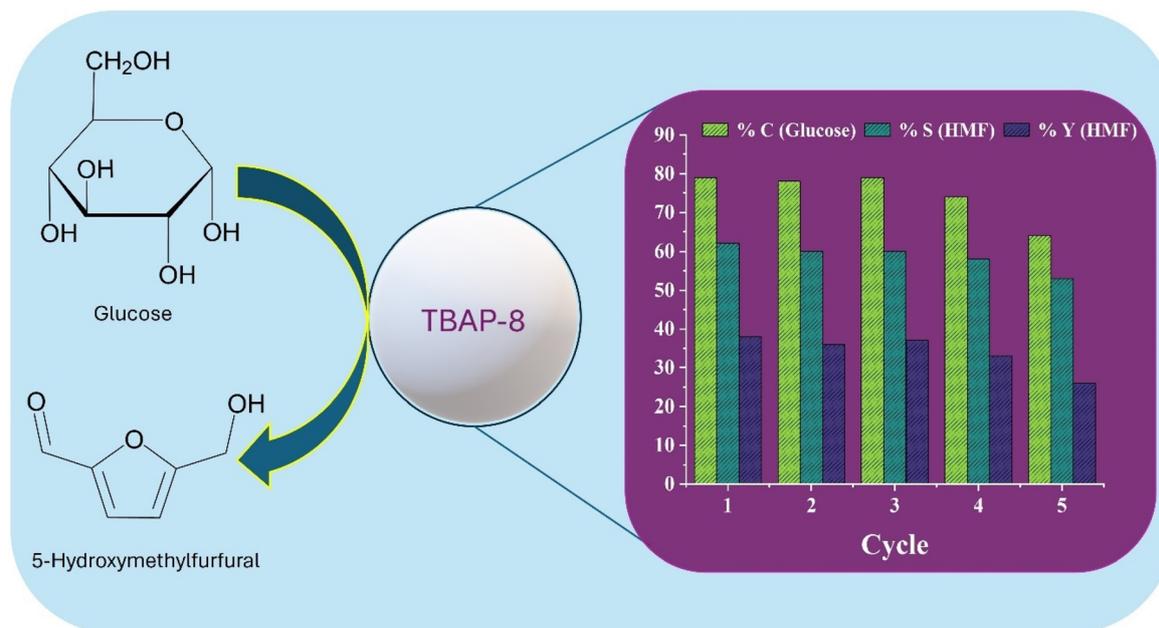
Fig. 10 Recyclability of TBAP-8 in glucose conversion to HMF. Reaction conditions: glucose = 1 g, DMSO = 10 mL, catalyst quantity = 200 mg (20 wt%), temperature = 160 °C, time = 12 h.

4. Conclusion

HMF was obtained by the dehydration of glucose using a modified hydroxyapatite called the *tert*-butoxy apatite catalyst. The cyclic intermediate is formed by the interaction of the hydroxyl group in the glucopyranose ring with Ca^{2+} (Lewis acid) to undergo isomerization to fructose. The fructose formed subsequently undergoes dehydration in the presence of hydrogenophosphates (Brønsted acid) to finally afford HMF. The yield of HMF was 48% with 20 wt% of catalyst at a temperature of 160 °C in 12 h. The catalyst can be used for five cycles. Moreover, a liquid–liquid extraction technique was developed to separate HMF from the reaction mixture.

Conflicts of interest

There are no conflicts to declare.

Data availability

The amount of humin formed in different parameter studies, HPLC chromatograms, and an FTIR plot are provided in the SI. See DOI: https://doi.org/10.1039/d5dt01450f.

Acknowledgements

References

1 O. He, Y. Zhang, P. Wang, L. Liu, Q. Wang, N. Yang, W. Li, P. Champagne and H. Yu, *Catalysts*, 2021, **11**, 1–13.

2 P. A. Kamble, M. L. Kantam and V. K. Rathod, *ChemistrySelect*, 2021, **6**, 6601–6606.

3 F. Parveen and S. Upadhyayula, *Fuel Process. Technol.*, 2017, **162**, 30–36.

4 P. A. Kamble, C. P. Vinod, V. K. Rathod and M. L. Kantam, *Catal. Today*, 2023, **408**, 36–49.

5 X. Qi, M. Watanabe, T. M. Aida and R. L. Smith, *Catal. Commun.*, 2008, **9**, 2244–2249.

6 P. A. Kamble, C. P. Vinod, V. K. Rathod and M. L. Kantam, *Appl. Catal., A*, 2024, **674**, 119621.

7 S. P. Teong, G. Yi and Y. Zhang, *Green Chem.*, 2014, **16**, 2015–2026.

8 W. Fan, C. Verrier, Y. Queneau and F. Popowycz, *Curr. Org. Synth.*, 2019, **16**, 583–614.

9 A. D. Patel, J. C. Serrano-Ruiz, J. A. Dumesic and R. P. Anex, *Chem. Eng. J.*, 2010, **160**, 311–321.

10 R. J. Van Putten, J. C. Van Der Waal, E. De Jong, C. B. Rasrendra, H. J. Heeres and J. G. De Vries, *Chem. Rev.*, 2013, **113**, 1499–1597.

11 Y. Román-Leshkov, J. N. Chheda and J. A. Dumesic, *Science*, 2006, **312**, 1933–1937.

12 J. N. Chheda, Y. Román-Leshkov and J. A. Dumesic, *Green Chem.*, 2007, **9**, 342–350.

13 A. I. Torres, P. Daoutidis and M. Tsapatsis, *Energy Environ. Sci.*, 2010, **3**, 1560–1572.

14 A. Corma, S. Iborra and A. Velty, *Chem. Rev.*, 2007, **107**, 2411–2502.

15 I. Jiménez-Morales, A. Teckchandani-Ortiz, J. Santamaría-González, P. Maireles-Torres and A. Jiménez-López, *Appl. Catal., B*, 2014, **144**, 22–28.

16 X. Qi, M. Watanabe, T. M. Aida and R. L. Smith, *ChemSusChem*, 2009, **2**, 944–946.

17 M. Ohara, A. Takagaki, S. Nishimura and K. Ebitani, *Appl. Catal., A*, 2010, **383**, 149–155.

18 H. Yan, Y. Yang, D. Tong, X. Xiang and C. Hu, *Catal. Commun.*, 2009, **10**, 1558–1563.

19 J. Liu, H. Li, Y. C. Liu, Y. M. Lu, J. He, X. F. Liu, Z. B. Wu and S. Yang, *Catal. Commun.*, 2015, **62**, 19–23.

20 C. Mondelli, D. Ferri and A. Baiker, *J. Catal.*, 2008, **258**, 170–176.

21 K. Tõnsuaadu, M. Gruselle, F. Villain, R. Thouvenot, M. Peld, V. Mikli, R. Traksmaa, P. Gredin, X. Carrier and L. Salles, *J. Colloid Interface Sci.*, 2006, **304**, 283–291.

22 P. A. Kamble, C. P. Vinod, V. K. Rathod and M. Lakshmi Kantam, *ChemCatChem*, 2024, **16**, e202301590.

23 K. Kaneda and T. Mizugaki, *Energy Environ. Sci.*, 2009, **2**, 655–673.

24 K. Mori, M. Oshiba, T. Hara, T. Mizugaki, K. Ebitani and K. Kaneda, *Tetrahedron Lett.*, 2005, **46**, 4283–4286.

25 K. Mori, T. Hara, T. Mizugaki, K. Ebitani and K. Kaneda, *J. Am. Chem. Soc.*, 2003, **125**, 11460–11461.

26 Y. Masuyama, K. Yoshikawa, N. Suzuki, K. Hara and A. Fukuoka, *Tetrahedron Lett.*, 2011, **52**, 6916–6918.

27 M. Lakshmi Kantam, G. T. Venkanna, C. Sridhar and K. B. Shiva Kumar, *Tetrahedron Lett.*, 2006, **47**, 3897–3899.

28 J. Ichihara, A. Kambara, K. Iteya, E. Sugimoto, T. Shinkawa, A. Takaoka, S. Yamaguchi and Y. Sasaki, *Green Chem.*, 2003, **5**, 491–493.

29 A. Venugopal and M. S. Scurrell, *Appl. Catal., A*, 2003, **245**, 137–147.

30 M. Dessoudeix, U. J. Jáuregui-Haza, M. Heughebaert, A. M. Wilhelm, H. Delmas, A. Lebugle and P. Kalck, *Adv. Synth. Catal.*, 2002, **344**, 406–412.

31 S. Diallo-Garcia, M. Ben Osman, J. M. Krafft, S. Casale, C. Thomas, J. Kubo and G. Costentin, *J. Phys. Chem. C*, 2014, **118**, 12744–12757.

32 M. Ben Osman, S. Diallo Garcia, J. M. Krafft, C. Methivier, J. Blanchard, T. Yoshioka, J. Kubo and G. Costentin, *Phys. Chem. Chem. Phys.*, 2016, **18**, 27837–27847.

33 L. Silvester, J. F. Lamonier, J. Faye, M. Capron, R. N. Vannier, C. Lamonier, J. L. Dubois, J. L. Couturier, C. Calais and F. Dumeignil, *Catal. Sci. Technol.*, 2015, **5**, 2994–3006.

34 A. Chareonlimkun, V. Champreda, A. Shotipruk and N. Laosiripojana, *Fuel*, 2010, **89**, 2873–2880.

35 A. Chareonlimkun, V. Champreda, A. Shotipruk and N. Laosiripojana, *Bioresour. Technol.*, 2010, **101**, 4179–4186.

36 M. Watanabe, Y. Aizawa, T. Iida, R. Nishimura and H. Inomata, *Appl. Catal., A*, 2005, **295**, 150–156.

37 R. Tomer and P. Biswas, *Catal. Today*, 2022, **404**, 219–228.

38 K. Li, M. Du and P. Ji, *ACS Sustainable Chem. Eng.*, 2018, **6**, 5636–5644.

39 J. Wang, J. Ren, X. Liu, J. Xi, Q. Xia, Y. Zu, G. Lu and Y. Wang, *Green Chem.*, 2012, **14**, 2506–2512.

40 Z. Zhang, B. Du, L. J. Zhang, Y. X. Da, Z. J. Quan, L. J. Yang and X. C. Wang, *RSC Adv.*, 2013, **3**, 9201–9205.

41 A. Herbst and C. Janiak, *New J. Chem.*, 2016, **40**, 7958–7967.

42 L. Zhang, G. Xi, Z. Chen, Z. Qi and X. Wang, *Chem. Eng. J.*, 2017, **307**, 877–883.

43 B. M. Choudary, C. Sridhar, M. L. Kantam, G. T. Venkanna and B. Sreedhar, *J. Am. Chem. Soc.*, 2005, **127**, 9948–9949.

44 D. Gupta, E. Ahmad, K. K. Pant and B. Saha, *RSC Adv.*, 2017, **7**, 41973–41979.

45 K. C. Vinoth Kumar, T. Jani Subha, K. G. Ahila, B. Ravindran, S. W. Chang, A. H. Mahmoud, O. B. Mohammed and M. A. Rathi, *Saudi J. Biol. Sci.*, 2021, **28**, 840–846.

46 S. C. Wu, H. C. Hsu, H. F. Wang, S. P. Liou and W. F. Ho, *Molecules*, 2023, **28**, 4926.

47 Y. Essamlali, O. Amadine, A. Fihri and M. Zahouily, *Renewable Energy*, 2019, **133**, 1295–1307.

48 J. J. Lovón-Quintana, J. K. Rodriguez-Guerrero and P. G. Valença, *Appl. Catal., A*, 2017, **542**, 136–145.

49 T. Q. Tran, D. Pham Minh, T. S. Phan, Q. N. Pham and H. Nguyen Xuan, *Chem. Eng. Sci.*, 2020, **228**, 115975.

50 L. Borkowski, A. Przekora, A. Belcarz, K. Palka, G. Jozefaciuk, T. Lübek, M. Jojczuk, A. Nogalski and G. Ginalska, *Mater. Sci. Eng., C*, 2020, **116**, 111211.

51 A. Sharifnabi, B. Eftekhari Yekta, M. H. Fathi and M. Hossainalipour, *J. Sol-Gel Sci. Technol.*, 2015, **74**, 66–77.

52 N. Montazeri, R. Jahandideh and E. Biazar, *Int. J. Nanomed.*, 2011, **6**, 197–201.

53 Z. Fereshteh, M. Fathi and R. Mozaffarinia, *J. Cluster Sci.*, 2015, **26**, 1041–1053.

54 M. Wei, J. H. Evans and L. Gréndahl, *J. Mater. Sci. Mater. Med.*, 2003, **14**, 311–320.

55 K. Sangeetha, M. Ashok and E. K. Girija, *Ceram. Int.*, 2019, **45**, 12860–12869.

56 M. A. El-Aal, H. M. Ali and S. M. Ibrahim, *ACS Omega*, 2022, **7**, 26777–26787.

57 S. Yuvaraj, N. Muthukumarasamy, M. Flores, G. Rajesh, K. M. Paraskevopoulos, G. K. Pouroutzidou, G. S. Theodorou, K. Ioannidou, L. Lusvarghi, D. Velauthapillai and C. P. Yoganand, *Vacuum*, 2021, **190**, 110300.

58 J. L. Xu and K. A. Khor, *J. Inorg. Biochem.*, 2007, **101**, 187–195.

59 Y. Liu and F. M. Kerton, *Pure Appl. Chem.*, 2021, **93**, 463–478.

60 S. Mahala, S. M. Arumugam, S. Kumar, D. Singh, S. Sharma, B. Devi, S. K. Yadav and S. Elumalai, *ChemCatChem*, 2021, **13**, 4787–4798.

61 S. Caratzoulas and D. G. Vlachos, *Carbohydr. Res.*, 2011, **346**, 664–672.

62 N. Nikbin, S. Caratzoulas and D. G. Vlachos, *ChemCatChem*, 2012, **4**, 504–511.

63 G. Yang, E. A. Pidko and E. J. M. Hensen, *J. Catal.*, 2012, **295**, 122–132.